

# Temperature Dependence of the Primary Donor Triplet State g-Tensor in Photosynthetic Reaction Centers of *Rhodobacter sphaeroides* R-26 Observed by Transient 240 GHz Electron Paramagnetic Resonance

Ronghui Zeng,<sup>†</sup> Johan van Tol,<sup>‡</sup> Amanda Deal,<sup>§</sup> Harry A. Frank,<sup>§</sup> and David E. Budil\*,<sup>†</sup>

Department of Chemistry and Chemical Biology, Northeastern University, Boston Massachusetts 02115, National High Magnetic Field Laboratory, Center for Interdisciplinary Magnetic Resonance, Florida State University, Tallahassee, Florida 32310, and Department of Chemistry, U-3060, University of Connecticut, Storrs, Connecticut 06269

Received: July 16, 2002; In Final Form: February 5, 2003

We report time-resolved 240 GHz EPR spectra of the primary donor triplet state  $^3\text{P}$  from photosynthetic reaction centers of *Rhodobacter sphaeroides* R26.1 as a function of temperature in the range 10–230 K. The data allow the determination of the principal g-tensor values and the principal axes directions of the  $^3\text{P}$  g-tensor with respect to its zero-field axes. The g-tensor measured at 240 GHz differs appreciably from previous measurements of  $^3\text{P}$  at lower frequencies and also differs from that of the cation radical state  $\text{P}^+$ , which has previously been characterized at high frequencies. In contrast to  $\text{P}^+$ , the  $^3\text{P}$  state exhibits significant temperature dependence in its g-tensor, particularly in the directions of the principal axes, which appear to rotate by about  $30^\circ$  around the  $x$  principal axis over the temperature range studied. The  $^3\text{P}$  yield anisotropy first observed by Boxer and co-workers at high field using photoselection methods is also evident in the high-field EPR spectrum as a significant variation of intensity across the spectrum. This variation is analyzed in terms of two models. The first model explicitly includes the evolution of the precursor radical pair but leads to significant ambiguities in the assignment of radical pair structural parameters. The second model utilizes only two ad hoc parameters to account for the yield anisotropy, which greatly reduces fitting parameter correlations and improves the accuracy and reliability with which the  $^3\text{P}$  magnetic parameters are determined.

## Introduction

Electron paramagnetic resonance (EPR) studies have played a central role in elucidating the electronic structure of the cofactors in the photosynthetic reaction center (RC) that are involved in the primary light-induced electron-transfer reaction. High-frequency electron paramagnetic resonance (HF-EPR) at quasioptical wavelengths<sup>1–3</sup> has provided new insight into the structure of organic radicals by resolving the electronic g-tensors.

Most quasioptical EPR studies of RCs have focused on radical ions in different organisms.<sup>4–11</sup> Another paramagnetic state that has yielded much information about the photodynamics of the RC at conventional EPR frequencies is the primary donor triplet state  $^3\text{P}^*$ ,<sup>12–16</sup> which is formed by back-reaction of the primary radical pair ( $\text{P}^+ \text{BPh}^-$ ) in RCs when secondary electron transfer beyond the bacteriopheophytin (BPh) acceptor is blocked. We have reported preliminary observations of  $^3\text{P}^*$  by 240 GHz EPR<sup>17</sup> and two groups have subsequently published spectra of  $^3\text{P}^*$  at the significantly lower frequencies of 95 GHz<sup>18</sup> and 130 GHz.<sup>19</sup> In this work we present high-frequency (240 GHz) EPR spectra of the primary donor triplet state  $^3\text{P}$  from photosynthetic reaction centers of *Rhodobacter sphaeroides* R26.1 as a function of temperature. The spectra exhibit several striking new features in comparison with spectra of  $^3\text{P}$  at lower frequencies, including a pronounced asymmetry of the spectrum, a difference in the spin polarization pattern, and an unusual variation in intensity across the spectrum. This variation most likely reflects anisotropy

in the yield of  $^3\text{P}$  at high field, which was first demonstrated by the photoselection studies of Boxer and co-workers.<sup>20–22</sup> Orientation dependence in the triplet yield results from g-factor anisotropy in the precursor radical pair, which dominates the rate of radical pair singlet–triplet intersystem crossing at high fields. Thus, analysis of the high-field EPR line shape of  $^3\text{P}$  should in principle provide structural information about the precursor radical pair.

However, analysis of the results using a model that explicitly takes the precursor radical pair g-anisotropy into account leads to large ambiguity in the large number of parameters required, and a wide range of possible solutions that fit the low-temperature  $^3\text{P}$  spectrum. An alternative model that utilizes two phenomenological yield ratio parameters gives a unique and very accurate fit the low-temperature experimental line shape, at the expense of limiting structural information about the precursor radicals. The use of this second model to account for yield anisotropy effects makes it possible to fully determine the  $^3\text{P}$  g-tensor; that is, the reduced parameter set allows one to determine the principal g-values as well as the three additional parameter that specify the g-tensor axis directions relative to the triplet zero-field axes.

With the resolution of g-tilt in the high-field spectrum, the principal g-values of  $^3\text{P}$  determined at 240 GHz differ appreciably from previous measurements at 130 GHz and lower frequencies. The g-tensor of the  $^3\text{P}$  state also differs considerably from that of the cation radical state  $\text{P}^+$  in both the principal g-values and the principal axis orientations. Most significantly, although the  $\text{P}^+$  g-tensor appears to be temperature-independent

<sup>†</sup> Northeastern University.

<sup>‡</sup> Florida State University.

<sup>§</sup> University of Connecticut.

over a wide temperature range,<sup>5</sup> that of  $^3\text{P}$  exhibits a notable temperature dependence in the range 10–230 K. Specifically, the **g**-axes appear to be significantly tilted from the zero-field axes at low temperature, but rotate closer to the zero-field axes as the temperature approaches 230 K. Possible explanations for these differences will be discussed.

## Experimental Section

Cells from *Rb. sphaeroides* R26.1 were grown anaerobically and photosynthetically in modified Hutner's medium. RCs were prepared according to the method of Wraight,<sup>23</sup> and ubiquinone was removed from the RCs by the procedure of Okamura et al.<sup>24</sup> The RCs were concentrated to OD = 5 cm<sup>-1</sup> at 532 nm. A 20% (wt/vol) solution of poly(vinyl alcohol) (PVA, Sigma, average mol. wt. 49,000) was mixed with the RC solution in a 4:1 ratio and dried on a plastic microscope cover slip at room temperature under dry nitrogen to form a film approximately 0.5–0.8 mm thick. The films were cut into 5 mm diameter circles using a standard hole punch tool, and approximately 10 circles were stacked tightly together to form a column about 6 mm long.

EPR spectra were acquired at 240 GHz on a multifrequency quasioptical transient EPR spectrometer at the National High Magnetic Field Laboratory that has been described elsewhere.<sup>25</sup> The spectrometer uses conventional cw superheterodyne detection,<sup>26</sup> but is implemented using quasioptics such as off-axis elliptical mirrors and wire grids<sup>27,28</sup> that enable virtually lossless free-space propagation and polarization diplexing of the EPR signal. The source consists of a 120 GHz phase-locked Gunn diode that can be multiplied to 240 or 360 GHz. A reference oscillator, also a phase-locked Gunn-diode with appropriate multipliers, is tuned to 6 GHz below the source. The source power passes through a ferrite isolator and a Martin-Puplett interferometer before entering an oversized corrugated cylindrical waveguide that conducts the power from the top of the variable temperature cryostat to the sample. The detection system is based on Schottky diodes and has a 1 GHz bandwidth. The room-temperature CW sensitivity at 240 GHz is of the order of 10<sup>11</sup> spins/gauss without a cavity (1 Hz bandwidth).

The sample holder was a nonresonant cylindrical cell approximately 5 mm in diameter and 8 mm in length machined into a block of aluminum and situated to be coaxial with the spectrometer field. One end of the cylinder was attached to a waveguide flange at the narrow end of a horn antenna that served as the transition from the oversized waveguide diameter to the sample cell diameter. Optical excitation is achieved with laser pulses from a 5 ns Q-switched Nd:YAG laser that is frequency-doubled to 532 nm with a 10 Hz repetition rate. Light is conducted into the magnet bore via a quartz light guide, and directed by a prism into a 4 mm aperture in the side of the sample cylinder.

Time-resolved data were acquired by slowly sweeping the magnetic field and averaging 16 shots for both the in-phase and quadrature EPR signals in a digital oscilloscope, which were then digitally integrated over time gates of 2  $\mu\text{s}$  (5  $\mu\text{s}$  for the data at 30 K). All spectra presented here consist of a single field sweep of 12 to 24 min. To minimize effects due to spin relaxation and decay to the ground state, only the first time gate after the laser pulse was used for line shape analysis. A MgO: Mn<sup>2+</sup> field calibration run was made immediately before the experiments; however, there was no internal **g**-standard, leaving a field uncertainty of 0.5 mT due to power-supply instability. Both quadrature signals were detected simultaneously, allowing post-experiment phase-correction.

Phase-corrected spectra were analyzed using Levenberg–Marquardt nonlinear least-squares minimization based on a line shape program for randomly oriented, spin-polarized triplet states with yield anisotropy, which were written locally in MATLAB.<sup>29</sup> Fitting parameters included the magnetic properties of  $^3\text{P}$ : specifically, its zero-field splittings  $D$  and  $E$ , principal **g**-values  $g_x$ ,  $g_y$ , and  $g_z$ , inhomogeneous line width  $\Delta H_{\text{pp}}$ , (the first-derivative peak-to-peak Gaussian line width), and “**g**-tilt angles” (i.e., the Euler angles between the zero-field axes and the **g**-matrix principal axes, according to the *y*-convention described by Zare<sup>30</sup>). The rationale for including the **g**-tilt parameters in the fitting procedure is discussed below. The values of  $D$  and  $E$  at each of the temperatures studied were fixed at values obtained from the literature.<sup>31,32</sup> Both sign conventions for the  $E$  parameter may be found in the literature. In this work we adopt the convention  $E < 0$  for  $^3\text{P}$ , according to which the Y peaks of the triplet spectrum appear between the X and Z peaks for both the  $0 \rightarrow +1$  and  $-1 \rightarrow 0$  transition manifolds, and  $g_x > g_y > g_z$  for the associated **g**-tensor axes. This convention also places the zero-field X axis closest to the direction of the transition dipole of the lower exciton band of the primary donor dimer ( $Q_y$ ).

In addition to the  $^3\text{P}$  magnetic parameters, the line shape program contained parameters describing the orientation dependence of the triplet yield. Two basic models were applied to describe this orientation dependence, which we will refer to as the “yield ratio model” (YRM) and the “radical pair model” (RPM).

The YRM utilizes a simple ad hoc characterization of the triplet yield orientation dependence using two anisotropy parameters,  $r_x \equiv P_x/P_z$ , and  $r_y \equiv P_y/P_z$ , where  $P_x$ ,  $P_y$  and  $P_z$  are the relative populations of the  $T_0$  spin sublevel when the spectrometer field is aligned with the X, Y, and Z zero-field directions, respectively. Thus, for a given orientation of  $B_0$  in the zero-field frame specified by the polar angles  $(\theta, \phi)$ , the relative population of the  $T_0$  spin sublevel is given by

$$P_{T_0} = \frac{(r_x \cos^2 \phi + r_y \sin^2 \phi) \sin^2 \theta + \cos^2 \theta}{r_x^2 + r_y^2 + 1} \quad (1)$$

The RPM takes explicit account of the anisotropic magnetic interactions in the precursor radical pair  $\text{P}^+ \text{I}^-$  that lead to an orientation-dependent rate of intersystem crossing.<sup>22</sup> A closed-form expression for the triplet yield dependence upon the polar angles  $(\beta, \gamma)$  of  $B_0$  in the zero-field frame similar to that given by Till and Hore<sup>33</sup> was obtained by algebraically solving the stochastic Liouville equation for radical pair evolution in the  $S$ ,  $T_0$  state basis.

$$\Phi_T(\beta, \gamma) = \frac{k_T \xi \delta^2}{\xi^4 + \xi^2 \eta^2 - \zeta^2 \epsilon^2}$$

where  $\eta^2 = \delta^2 + \epsilon^2 + \zeta^2$ ,  $\delta = (2\Delta\mathbf{g}(\beta, \gamma)B_0 + \Delta A_{\text{eff}})$ ,  $\epsilon = 4J_{\text{PI}} + d_{\text{PI}}(\cos^2 \theta - (1/3))$ ,  $\zeta = k_{\text{T}} - k_{\text{S}}$ ,  $\xi = k_{\text{T}} + k_{\text{S}}$ ,  $2J$  is the exchange interaction in the radical pair,  $d_{\text{PI}}$  is the parameter characterizing the dipolar coupling between the electron spins,  $\Delta\mathbf{g}(\beta, \gamma)$  is the orientation-dependent **g**-factor difference between  $\text{P}^+$  and  $\text{I}^-$ ,  $\Delta A_{\text{eff}}$  is the difference in effective nuclear hyperfine fields between the two radicals, and  $k_{\text{S}}$  and  $k_{\text{T}}$  are the decay rate constants for singlet- and triplet-correlated radical pair, respectively. The quantities  $\Delta\mathbf{g}$  and  $\theta$  may be calculated for each field orientation using parameters for the orientations of the **g**-axis systems of  $\text{P}^+$  and  $\text{I}^-$ , specified by their Euler angles relative to the molecular structure (unit cell axes).

**TABLE 1: Magnetic Parameters of the  $^3\text{P}$  State in RCs of *Rb. sphaeroides* R-26 as a Function of Temperature**

$T$ (K)	$D^a$ ( $\text{cm}^{-1}$ )	$E^a$ ( $\text{cm}^{-1}$ )	$g_x^b$	$g_y^b$	$g_z^b$	$\Delta H_{\text{pp}}^c$ (G)	$r_x^d$	$r_y^d$	$g$ -tilt angles <sup>e</sup> (degrees)		
									$\alpha$	$\beta$	$\gamma$
10	187.90	−31.79	2.00388	2.00268	2.00183	17.4	0.49	0.94	80	26	−108
			2.00355	2.00277	2.00202	17.4	0.50	0.88	0	0	0
30	187.90	−31.79	2.00391	2.00265	2.00181	17.4	0.49	0.88	99	16	−123
			2.00355	2.00277	2.00202	16.8	0.50	0.83	0	0	0
60	188.20	−32.00	2.00393	2.00263	2.00181	19.2	0.48	0.87	105	12	−127
			2.00356	2.00274	2.00202	17.4	0.49	0.77	0	0	0
100	189.30	−32.30	2.00384	2.00265	2.00184	17.2	0.43	0.81	153	6	−170
			2.00358	2.00275	2.00199	20.5	0.44	0.69	0	0	0
160	192.20	−33.30	2.00387	2.00264	2.00179	25.2	0.43	0.80	−150	9	134
			2.00364	2.00273	2.00192	25.0	0.45	0.73	0	0	0
230	197.81	−34.99	2.0040	2.0030	2.0018	26.4	0.39	0.77	−154	16	158
			2.0038	2.0031	2.0019	26.4	0.24	0.95	0	0	0

<sup>a</sup> Zero-field splitting parameters fixed at temperature-dependent values obtained from refs 31 and 32. <sup>b</sup> Average relative uncertainty in  $g$ -values is  $4 \times 10^{-5}$  from 10 to 100 K,  $1 \times 10^{-4}$  at 160 K, and  $3 \times 10^{-4}$  at 230 K. The uncertainty in field calibration leads to an additional uncertainty of  $\pm 0.00010$  in the absolute mean  $g$ -value. <sup>c</sup> Reported  $g$ -value uncertainties are relative values. The uncertainty in field calibration leads to an additional error of  $\pm 0.00010$  in the absolute mean  $g$ -value. <sup>d</sup> Peak-to-peak line width of the first derivative Gaussian line. Average uncertainty is 1.5 G. <sup>e</sup> Average uncertainty in yield ratio parameters is 0.02 from 10 to 100 K, 0.05 at 160 K, and 0.09 at 230 K.

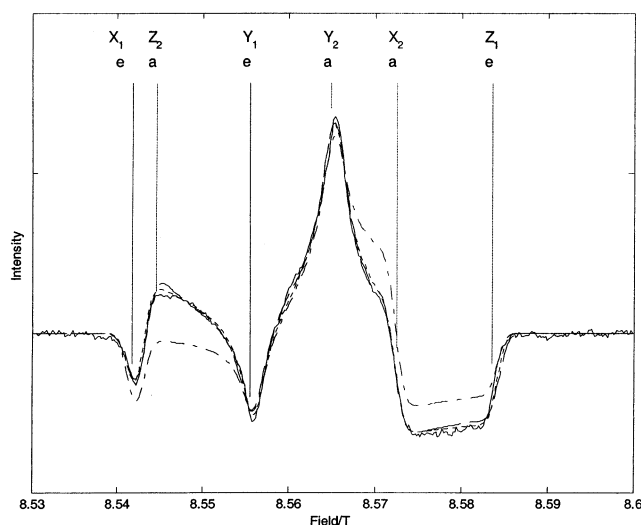


**Figure 1.** Time-resolved 240 GHz spectrum of  $^3\text{P}$  in RCs of *Rb. sphaeroides*, at 30 K, showing the polarization pattern **EAEAAE**, where **E** stands for emission and **A** for absorption (solid line). The dashed line shows the theoretical line shape calculated using the radical pair model and parameters given in the text. The dotted line shows a nearly identical line shape calculated using the yield ratio model and parameters in Table 1. The dash-dotted line shows the line shape calculated using the magnetic parameters, but assuming isotropic  $T_0$  polarization. X, Y, and Z peaks are labeled for the  $T_0 \rightarrow T_{-1}$  transitions (1) and the  $T_0 \rightarrow T_{+1}$  transitions (2).

Data were fitted in the absorption mode and also in the first derivative mode after applying a Savitzky-Golay filter<sup>34</sup> with a polynomial order of 3 and a window size of 21 to carry out numerical differentiation of the experimental spectrum. Parameter uncertainties were estimated from the curvature matrix of the fitting procedure using the  $F$ -distribution.<sup>35</sup> The phase of the spectrum (i.e., absorption vs dispersion) was allowed to vary in the fitting procedure to correct for any small errors in the experimental phase correction described above.

## Results

Figure 1 shows the nonderivative spectrum of  $^3\text{P}$  at 30 K, integrated over the first 5  $\mu\text{s}$  after the laser pulse. The spectrum is considerably less symmetric than at 9 GHz, but still exhibits six features associated with the X, Y, and Z zero-field principal axis directions for each of the two allowed spin transitions ( $m_S = -1 \rightarrow 0$  and  $m_S = 0 \rightarrow +1$ ) in the triplet state. This figure

exhibits several of the new features that are observed in the 240 GHz spectrum of  $^3\text{P}$ , as we describe below.

**Spin Polarization Pattern.** The features of the  $^3\text{P}$  EPR spectrum exhibit a pattern of emission (E) and absorption (A) that has been ascribed to preferential population of the  $m_S = 0$  spin sublevel ( $T_0$ ) via radical pair intersystem crossing in studies at 9 GHz.<sup>36</sup> However, in contrast to the pattern AEEAAE that is observed at conventional frequencies up to 130 GHz,<sup>19</sup> the pattern EAEAAE appears in the 240 GHz spectrum, as shown in Figure 1. This occurs because the  $g$ -value associated with the zero-field X-axis (defined, as noted above, according to the  $E < 0$  convention) is larger than the  $g$ -value associated with the zero-field Z axis, reversing the order of the  $X_{-1 \rightarrow 0}$  and  $Z_{0 \rightarrow +1}$  peaks at higher field. This peak crossing significantly enhances the sensitivity of the 240 GHz spectra to temperature-dependent changes in the  $g$ -tensor of  $^3\text{P}$ , and to tilting of the  $g$ -tensor principal axes away from the zero-field axis system, as discussed in greater detail below.

**Yield Anisotropy.** A second important characteristic of the 240 GHz  $^3\text{P}$  spectrum is its marked deviation from an isotropic  $T_0$  -polarized pattern, such as is observed at 9 GHz. The dash-dotted line in Figure 1 shows the theoretical 240 GHz EPR line shape of  $^3\text{P}$  assuming isotropic  $T_0$  polarization, which differs significantly from the experimental line shape. This comparison clearly illustrates that, although  $^3\text{P}$  is still populated entirely in the  $T_0$  spin sublevel, the EPR intensity across the high-field spectrum varies significantly.

The experimental spectrum at 30 K was fitted very well using either the RPM or the YRM to model yield anisotropy. The dotted line in Figure 1 shows a fit to the 30 K data using the YRM with the parameters given in Table 1. The zero-field splittings shown in Table 1 were fixed at values obtained from the literature,<sup>32</sup> and all other parameters were varied. The least-squares line shape for the YRM (dotted line) is in excellent agreement with the experimental spectrum, and nearly identical to the line shape obtained from RPM using the same magnetic parameters for  $^3\text{P}$  (shown by the dashed line, cf. below).

For the RPM, several of the model parameters were fixed at values obtained from the literature, as follows (all angles are given in radians). The principal  $g$ -values of  $\text{P}^+$  were set at ( $g_x = 2.00323$ ,  $g_y = 2.00241$ ,  $g_z = 2.00197$ ),<sup>5</sup> and the orientations of the  $\text{P}^+$   $g$ -axes relative to the zero-field axes were calculated from the reported orientations of the  $^3\text{P}$  zero-field axes<sup>37</sup> and the Euler angles ( $\alpha_P, \beta_P, \gamma_P$ ) = (2.584, 0.400, −2.623) of the  $\text{P}^+$   $g$ -axes relative to the symmetry axes of the P dimer. The



data reported in ref.<sup>37</sup> has been adapted to the convention defined by Prisner *et al.*<sup>38</sup> for the symmetry axes of the P dimer, in which the  $x$  axis lies along the  $Q_y$  optical transition dipole of the molecule and  $z$  is normal to the average plane of the dimer. The dimer symmetry axes were determined directly from the molecular structure (IAIJ, reference<sup>39</sup>) to obtain the transformation from the unit cell into the zero-field frame:  $(\alpha_z, \beta_z, \gamma_z) = (-0.905, 1.411, 2.702)$ . This transformation was applied to other vectors estimated from the crystal structure as described below.

A consensus set of the remaining radical pair parameters was obtained from several reaction yield detected magnetic resonance (RYDMR) and magnetic field modulation of reaction yield (MARY) studies,<sup>40,41</sup> as follows:  $J_{\text{PI}} = +0.7$  mT,  $k_{\text{S}} = 0.02$  ns<sup>-1</sup>,  $k_{\text{T}} = 0.5$  ns<sup>-1</sup>. The dipolar interaction parameter  $d_{\text{PI}} = -0.5$  mT was taken to be the  $D$  value for two point dipoles located at the centers of  $\text{P}^+$  and  $\text{I}^-$  as determined from the crystal structure; the vector between these centers had polar angles  $(\theta_{\text{PI}}, \phi_{\text{PI}}) = (2.618, 0.867)$  in the unit cell frame. These radical pair parameters were not varied in the fitting procedure.

Fittings were initially attempted using only six parameters from the RPM model: three principal  $g$ -values and three angles specifying the  $g$ -axis directions of the  $\text{I}^-$  radical. The magnetic parameters for  $^3\text{P}$  were the same as those used in the YRM and the other radical pair parameters were fixed at the values noted above. To the best of our knowledge, no accurate measurement of the principal  $g$ -values of  $\text{I}^-$  in *Rb. sphaeroides* by high-field EPR is yet available. Therefore, the starting principal  $g$ -values for  $\text{I}^-$  were taken to be those measured in *R. viridis* by Dorlet *et al.*<sup>9</sup> ( $g_x = 2.00437$ ,  $g_y = 2.00340$ ,  $g_z = 2.00239$ ) and the starting  $g$ -axis orientations were estimated from the crystal structure as follows:  $z$  was taken as the normal to the average plane of the I molecule,  $x$  as the projection of the  $\text{N}_\text{A} \rightarrow \text{N}_\text{C}$  vector onto the plane, and  $y$  as the projection of the  $\text{N}_\text{B} \rightarrow \text{N}_\text{D}$  vector onto the plane. This procedure gave the starting Euler angles  $(\alpha_1, \beta_1, \gamma_1) = (1.258, 0.958, 2.253)$  for the  $\text{I}^-$   $g$ -axes in the unit cell frame.

The best fit of the RPM to the 240 GHz data was obtained only when the  $\text{P}^+$   $g$ -axis orientations were varied in addition to the  $\text{I}^-$   $g$ -tensor parameters. For the fit shown by the dashed line in Figure 1, the following parameters were obtained:  $g_{\text{I}^-} = 2.00544$ ,  $g_{\text{I}^-} = 2.00304$ ,  $g_{\text{I}^-} = 2.00239$ ,  $(\alpha_1, \beta_1, \gamma_1) = (2.306, 0.616, 2.849)$ ,  $(\alpha_{\text{P}^+}, \beta_{\text{P}^+}, \gamma_{\text{P}^+}) = (1.750, 0.725, -2.360)$ . The  $g_x$  and  $g_y$  principal values obtained for  $\text{I}^-$  in *Rb. sphaeroides* R-26 were appreciably larger than those measured for *R. viridis*.<sup>9</sup> Although there is as yet no analogous high-field measurement for *Rb. sphaeroides* with which the principal values obtained by this analysis may be compared, it should be noted that the values are consistent with the difference in isotropic  $g$ -values estimated from 9 GHz spectra of the isolated  $\text{P}^+$  and  $\text{I}^-$  radicals in *Rb. sphaeroides*.<sup>42,43</sup> The most unusual results from the RPM are the principal  $g$ -axes of  $\text{I}^-$ : the  $z$ -axis is rotated by about 45° from the normal to the plane of the pheophytin macrocycle, which is difficult to rationalize on a physical basis.<sup>44</sup>

Although the RPM parameters given above correspond to a least-squares solution, acceptable fits to the data could be obtained over a very wide range of mutual  $g$ -axis orientations for the  $\text{P}^+$  and  $\text{I}^-$  radicals. Thus, the parameters describing these orientations exhibit a very high degree of correlation that prevents their accurate determination from a single spectrum. Paschenko *et al.*<sup>19</sup> also reported large ambiguity in the  $g$ -axis orientations of  $\text{P}^+$  and  $\text{I}^-$  in their fits to the 130 GHz spectrum of  $^3\text{P}$  at 10 K using the model of Till and Hore.<sup>33</sup> In contrast, the least-squares fit of the YRM corresponds to a unique pair of anisotropy ratio values. We find the YRM can reproduce

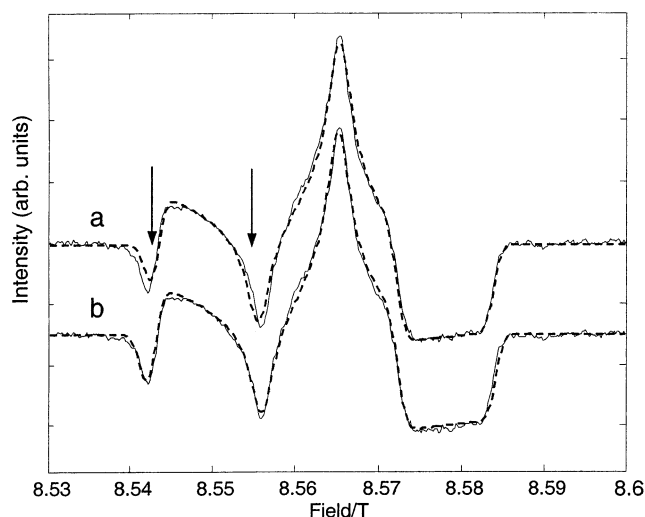


**Figure 2.** 240 GHz spectrum of  $^3\text{P}$  at 30 K (solid lines) overlaid with least-squares line shapes calculated using the yield ratio model (dashed lines) assuming (a) zero  $g$ -tilt angles and (b) tilt angles given in Table 1. Note the mismatch of the  $X_1$  and  $Y_1$  peaks calculated with zero  $g$ -tilt (indicated by arrows).

the spectrum calculated by the RPM very closely over a wide range of radical pair parameters, with little or no correlation between the yield ratio parameters. Although this model affords less information about the structural parameters of the radical pair, the great reduction in fitting parameter correlations allows the magnetic parameters of  $^3\text{P}$  to be determined much more accurately and reliably. The YRM model was therefore used for all subsequent data analysis.

**$g$ -Tilt.** Previous determinations of the  $^3\text{P}$  principal  $g$ -values have made the assumption that the  $g$ -axes are coincident with the zero-field axes of  $^3\text{P}$ .<sup>31,18,19</sup> There is no justification for this assumption on a physical basis, although it greatly simplifies the analysis and may have been necessary given the more limited resolution at 130 GHz and lower frequencies. It is known that the  $g$ -axes of the  $\text{P}^+$  state are significantly tilted away from the dimer symmetry axes,<sup>38,45</sup> which are coincident with the  $^3\text{P}$  zero-field axes to within 5°. Because the spin-orbit couplings (SOC) that give rise to  $g$ -anisotropy are likely to be at least qualitatively similar in the  $^3\text{P}$  and  $\text{P}^+$  states, this observation suggests that the  $g$ -tensor axes of  $^3\text{P}$  could also be tilted away from the zero-field axes. It should be noted, however, that despite qualitative similarities in the underlying spin-orbit interactions, both the principal axis orientations and the magnitudes of the principal  $g$ -values may differ significantly between  $^3\text{P}$  and  $\text{P}^+$ . These considerations motivate the inclusion of  $g$ -tilt angles in the line shape analysis.

Figure 2 illustrates the significant improvement in the least-squares fit (dashed lines) to the experimental 240 GHz line shape when  $g$ -tilt angles are included. The upper plot shows the least-squares fit obtained by varying the yield ratio parameters and principal  $g$ -values of  $^3\text{P}$  assuming zero axis tilt. With this assumption, it is not possible to match the splittings of the high-field and low-field  $x$  and  $y$  peaks of the 240 GHz spectrum simultaneously, and the least-squares algorithm fits the more intense high-field peaks at the expense of a mismatch of the low-field peaks (shown by arrows in Figure 2a). Because  $r_x$  and  $r_y$  were also optimized in this fit, it is clear that yield anisotropy effects also cannot fully account for the observed mismatch. The lower plot shows the significant improvement in the fit when  $g$ -tilt angles are allowed to vary, providing strong evidence for tilting of the  $g$ -tensor axes of  $^3\text{P}$ . Similar improvements in the fit with nonzero  $g$ -tilt are observed at temperatures

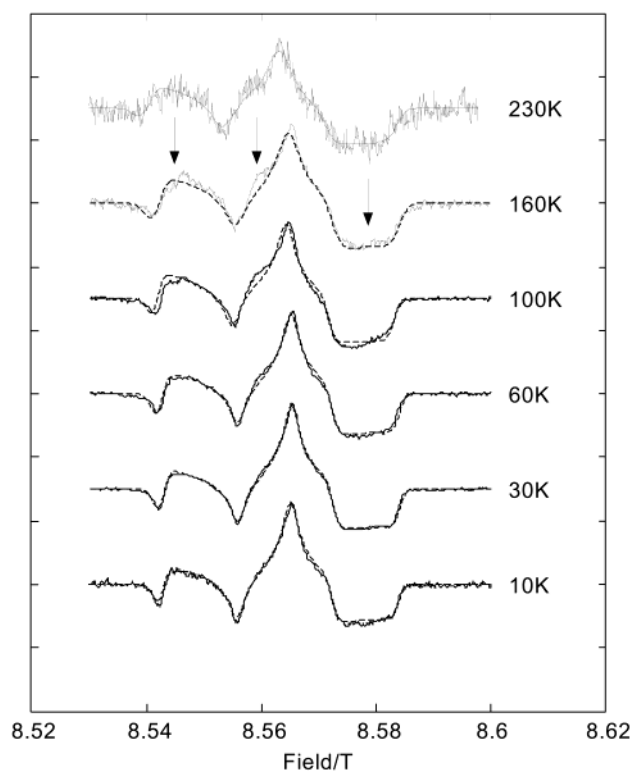


**Figure 3.** Time-resolved 240 GHz spectrum of  $^3\text{P}$  as a function of temperature. Dashed lines show least-squares fitted line shapes calculated using the yield ratio model with parameters in Table 1 for each temperature. Arrows show features not accounted for by the simple yield anisotropy model described in the text.

up to 100 K; at 160 and 230 K, the improvement in the  $\chi^2$  of the fit with  $\mathbf{g}$ -tilt was not statistically significant.

**Temperature Study.** The temperature dependence of the  $^3\text{P}$  signal between 10 and 230 K is shown in Figure 3. Dashed lines in the figure indicate least-squares line shapes calculated using the YRM at each temperature using the parameters given in Table 1. The spectra are consistent with the known temperature dependence of  $D$  and  $E$  zero-field splitting parameters<sup>31,32</sup> and inhomogeneous line width<sup>31</sup> observed by 9 GHz EPR and zero-field absorption detected magnetic resonance ADMR). Above 160 K, the signal intensity decreased dramatically because of faster spin relaxation, shorter lifetime, and lower quantum yield.

In addition to becoming wider and broader at higher temperatures, the 240 GHz spectrum of  $^3\text{P}$  exhibits two other important characteristics that are immediately apparent from Figure 3. First, the low-field emission-absorption feature observed at low temperature diminishes and then rapidly disappears above 160 K. The disappearance of this peak crossing provides a visual indication that the  $\mathbf{g}$ -tensor of  $^3\text{P}$  (including its principal values, its orientation, or both) is changing with temperature. Second, a number of new peaks appear in the spectra at 100 K and above, indicated by the arrows in the figure, that are not accounted for by the YRM fitting model. These will be discussed further below.

**Principal  $\mathbf{g}$ -Values of  $^3\text{P}$ .** Figure 4 shows a plot of the principal  $\mathbf{g}$ -values of  $^3\text{P}$  as a function of temperature. The closed symbols indicate values obtained with  $\mathbf{g}$ -tilt angles included in the fit, whereas the open symbols indicate those obtained with zero  $\mathbf{g}$ -tilt. In the latter case, a weak temperature dependence is observed in the apparent principal  $\mathbf{g}$ -values, such that  $g_x$  increases by approximately  $2 \times 10^{-4}$  and  $g_z$  decreases by approximately  $1 \times 10^{-4}$  upon going from 10 to 160 K. In the

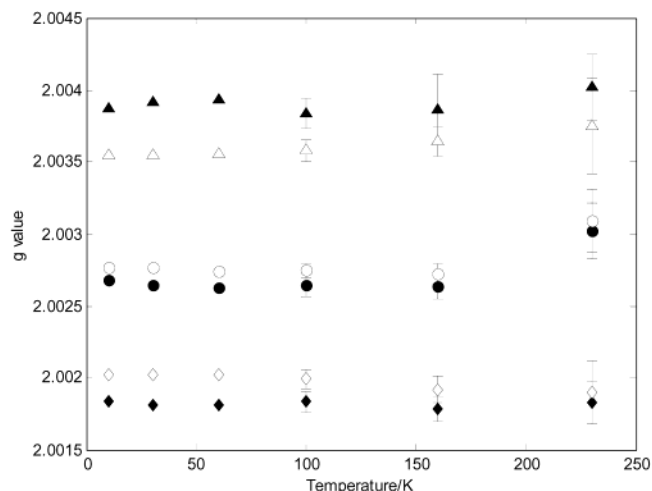


**Figure 4.** Principal  $\mathbf{g}$ -values ( $\blacktriangle$ )  $g_x$ , ( $\bullet$ )  $g_y$ , and ( $\blacklozenge$ )  $g_z$  of the  $^3\text{P}$  state as a function of temperature, as given in Table 1. Closed symbols show values obtained with  $\mathbf{g}$ -tilt angles and open symbols show values obtained assuming zero  $\mathbf{g}$ -tilt. Where error bars are not shown, the experimental uncertainty is less than or equal to the symbol size.

**TABLE 2: Direction Cosines of Principal Axes of the  $\mathbf{g}$ -Tensor in the Zero-Field Axis System of  $^3\text{P}$  in Reaction Centers of *Rb. sphaeroides* R-26 at 30 K**

$\mathbf{g}$ axes	zero-field axes		
	$x$	$y$	$z$
$g_x$	0.9102	-0.3859	0.1501
$g_y$	0.4118	0.8815	-0.2312
$g_z$	-0.0431	0.2722	0.9613

presence of  $\mathbf{g}$ -tilt, the principal  $\mathbf{g}$ -values obtained from the least-squares analysis are only very weakly dependent upon temperature, and the observed shifts of the turning points in the experimental spectrum arise from changes in the orientations of the principal  $\mathbf{g}$ -axes (cf. below). As the temperature increases, the principal  $\mathbf{g}$ -values in the zero-tilt case approach those obtained with  $\mathbf{g}$ -tilt. This trend appears to continue all the way up to 230 K, although the much larger experimental uncertainty at the very highest temperature makes this a tentative conclusion.

**Temperature Dependence of  $\mathbf{g}$ -Tilt Angles.** Figure 5a shows the  $^3\text{P}$   $\mathbf{g}$ -axis orientations relative to the zero-field frame at temperatures from 10 to 160 K as obtained from the line shape analysis. The orientations have experimental uncertainties of about  $8^\circ$  below 160 K, and  $15^\circ$  at 160 K. The Euler angles corresponding to each set of axes shown in Figure 5 are given in Table 1, and the direction cosines of the  $\mathbf{g}$ -axes at 30 K are given explicitly in Table 2. The most striking result shown in Figure 5 is that the  $\mathbf{g}$ -axes of  $^3\text{P}$  appear to be temperature-dependent, maintaining a nearly constant  $x$ -axis, whereas the other two axes rotate monotonically by  $\sim 30^\circ$  between 10 and 160 K.

Figure 5a also shows the principal  $\mathbf{g}$ -axis orientations of  $\text{P}^+$  (stars) in the zero-field frame of  $^3\text{P}$ , which were calculated from the reported orientations of the  $^3\text{P}$  zero field axes and  $\text{P}^+$   $\mathbf{g}$ -axes in the molecular symmetry frame.<sup>37,45</sup> We note that the axes shown in Figure 5 correspond to one of four possible solutions that are related by  $C_2$  rotations about each of the zero-field axes. The particular set shown was chosen from among the four possible solutions to give the largest absolute overlap with the corresponding  $\text{P}^+$  axes (defined as  $|\mathbf{x}_1 \cdot \mathbf{x}_2| + |\mathbf{y}_1 \cdot \mathbf{y}_2| + |\mathbf{z}_1 \cdot \mathbf{z}_2|$ ). It should further be noted that these experiments cannot distinguish between rotations of the zero-field axes and rotations of the  $\mathbf{g}$ -axes relative to the molecular frame, because only their relative orientation is determined.

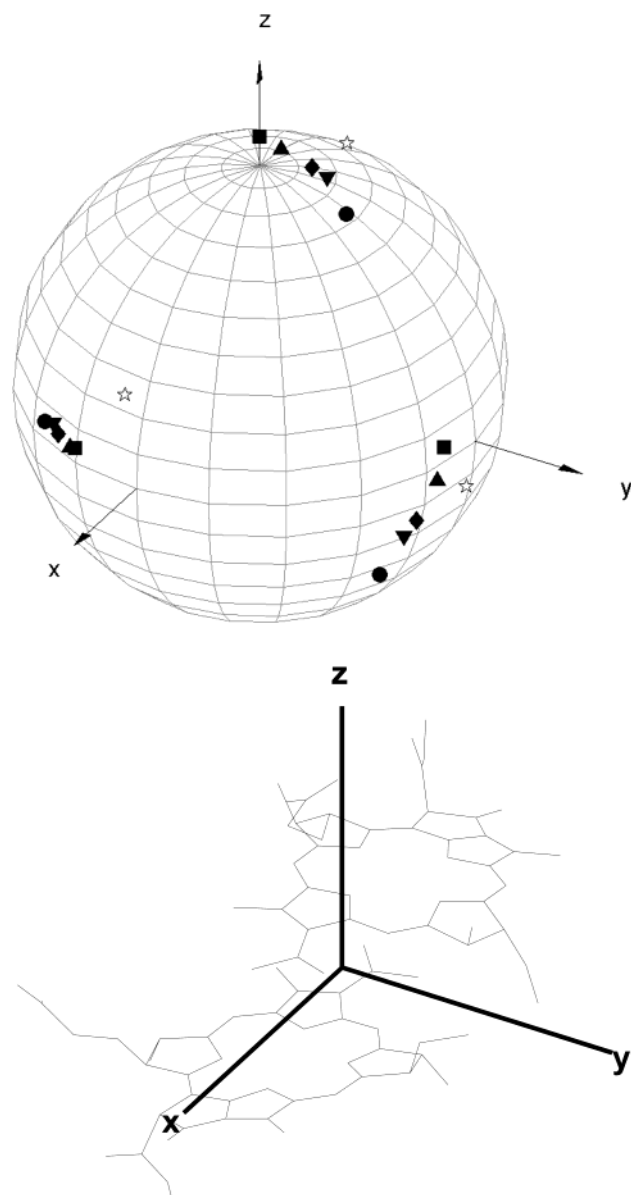


**Figure 5.** (a) Orientation of principal  $\mathbf{g}$ -tensor axes of  $^3\text{P}$  plotted on the unit sphere in the zero-field axis system of  $^3\text{P}$  (arrows) at temperatures of (●) 10 K, (▼) 30 K, (◆) 60 K, (▲) 100 K, (■) 160 K, and (☆) 230 K. Stars show the orientation of corresponding principal axes of the  $\text{P}^+$   $\mathbf{g}$ -tensor. (b) View of the molecular structure of the primary donor dimer from the same perspective shown in (a), with the zero-field axes indicated by arrows. The L-side of the dimer appears at the top of the diagram.

**TABLE 3: Comparison of Principal  $\mathbf{g}$ -Values Measured for the  $^3\text{P}$  State in RCs of *Rb. sphaeroides* R-26 at Different Frequencies and with the Principal  $\mathbf{g}$ -values of  $\text{P}^+$**

	ref	frequency (GHz)	temp (K)	$g_x$	$g_y$	$g_z$
$^3\text{P}$	31	9	15	2.0024	2.0024	2.0007
	18	95	1.2	2.00308	2.00238	2.00138
	19	130	40	2.0037	2.0028	2.0022
	this work	240	30	2.00391	2.00265	2.00181
	$\text{P}^+$	5	100–670	2.00323	2.00241	2.00197

## Discussion

Table 3 compares the  $^3\text{P}$  principal  $\mathbf{g}$ -values measured in the present work with previous measurements at lower frequencies. The results at 95 GHz and above all differ significantly from the values initially obtained by Hoff and Proskuryakov at

9 GHz;<sup>31</sup> in particular there is no evidence for the axial symmetry and a surprisingly low isotropic value reported by these authors. The present results at 240 GHz also differ appreciably from the measurements at 95 and 130 GHz, as shown in Table 3. Neglecting discrepancies in the isotropic  $\mathbf{g}$ -value, which may arise from differences in absolute field calibration, the 240 GHz measurement gives an overall  $\mathbf{g}$ -anisotropy that is significantly larger than that observed at lower frequencies; that is, the quantity  $(g_x - g_z)$  is larger by  $(4-6) \times 10^{-4}$ . This difference arises mainly from the tilt of the  $\mathbf{g}$ -axes that is resolved at the higher frequency.

The only previous mention of temperature dependence in the principal  $\mathbf{g}$ -values of  $^3\text{P}$  is the 9 GHz work of Hoff and Proskuryakov,<sup>31</sup> who reported an increase of  $17 \times 10^{-4}$  in  $g_x$  and  $20 \times 10^{-4}$  in  $g_z$  upon going from 15 to 293 K. In contrast, the 240 GHz data show the principal  $\mathbf{g}$ -values to be nearly constant or only weakly temperature-dependent over the temperature range studied, with no evidence for the large changes previously reported. It is clear that the much lower resolution available at 9 GHz greatly limits the reliability of the reported temperature effects.

The measurement of the  $\mathbf{g}$ -tensor of  $^3\text{P}$  offers a unique opportunity to compare the  $\mathbf{g}$ -tensors of two different states of the same molecule. As Table 3 shows, the principal  $\mathbf{g}$ -values, particularly  $g_x$  and  $g_y$ , are considerably larger than the corresponding values of  $\text{P}^+$ . The  $\mathbf{g}$ -axis orientations in the two states are also significantly different, as shown in Figure 5a. Although the set of  $^3\text{P}$   $\mathbf{g}$ -axes shown in this figure was arbitrarily selected from the four possibilities to be the one closest to the  $\text{P}^+$  axes, the important point is that the principal  $\mathbf{g}$ -axis orientations of  $\text{P}^+$  and  $^3\text{P}$  differ well beyond experimental uncertainty even in the case of closest overlap.

The observed differences between the  $\mathbf{g}$ -tensors of  $^3\text{P}$  and  $\text{P}^+$  may be rationalized in terms of the electronic structures of the two states. Whereas the unpaired spin in  $\text{P}^+$  occupies only the highest occupied molecular orbital (HOMO) of P, the second unpaired electron in  $^3\text{P}$  occupies the lowest occupied molecular orbital (LUMO); thus the  $\mathbf{g}$ -tensor of  $^3\text{P}$  reflects the properties of both HOMO and LUMO. Because the LUMO is singly occupied in the radical anion states, one might expect the  $\mathbf{g}$ -tensor of  $^3\text{P}$  to reflect the “average” properties of the radical cation and anion states in some sense. To our knowledge there is not yet available any direct comparison of the  $\mathbf{g}$ -tensors of monomeric bacteriochlorophyll anion and cation radicals in vitro at very high EPR fields; however, theoretical calculations suggest that the HOMO and LUMO of P should have very different symmetries.<sup>46–48</sup> Thus, it is reasonable to expect the  $\mathbf{g}$ -tensors of  $\text{P}^+$  and  $^3\text{P}$  to differ substantially in both their principal axis orientations and principal values.

Another important difference between the  $\mathbf{g}$ -tensors of  $^3\text{P}$  and  $\text{P}^+$  is the temperature dependence in the  $^3\text{P}$  state that is resolved at 240 GHz. It should be noted that some ambiguity remains in the interpretation of the temperature-dependent data. Specifically, the observed temperature-induced shifts in the “turning points” of the experimental spectrum data may be interpreted as changes in the principal  $\mathbf{g}$ -values, or as changes in the orientation of the  $\mathbf{g}$ -axes. Whereas the spectra below 100 K give clear evidence of  $\mathbf{g}$ -tilt (cf. Figure 2), the improvement of the fit with  $\mathbf{g}$ -tilt was not statistically significant at 160 K, and the  $\mathbf{g}$ -tilt could not be determined at 230 K. This uncertainty may result from the much lower signal-to-noise ratio at the higher temperatures; however, it could also reflect the fact that the least-squares  $\mathbf{g}$ -tensor axes orientations of  $^3\text{P}$  approach the zero-field axis orientations to within the experimental uncertainty at these



temperatures. Taken together with the very regular rotation of the **g**-axes shown in Figure 5a, however, these considerations favor interpreting the observed temperature shifts as a rotation of the **g**-tensor axes. In support of this conclusion, recent magnetophotoselection studies have shown that the triplet zero-field axes do not move relative to the optical transition axes of the RC chlorophylls below about 50 K.<sup>49</sup>

Regardless of which of the two interpretations discussed above actually applies, the data clearly demonstrate that there is some sort of temperature dependence in the **g**-tensor of <sup>3</sup>P. This contrasts with the observed behavior of the P<sup>+</sup> **g**-tensor, but parallels the temperature dependence that has previously been observed in the zero-field splittings<sup>31,32</sup> and inhomogeneous line width<sup>31</sup> of <sup>3</sup>P. This temperature dependence is difficult to rationalize solely on the basis of the molecular orbital arguments given above. Possible explanations for such behavior include (1) temperature-dependent conformational changes of the P molecule,<sup>50,51</sup> (2) temperature-dependent delocalization of triplet excitation onto an accessory bacteriochlorophyll,<sup>31,32,52</sup> and (3) SOC between <sup>3</sup>P and an electronic state with temperature-dependent energy, such as the first excited state of P.

The **g**-axes of <sup>3</sup>P, which are experimentally determined relative to the zero-field axes, may be compared directly with the molecular structure of the P dimer using the reported zero-field axis orientations relative to the structure.<sup>37</sup> Figure 5b shows the P structure drawn from the same viewpoint as Figure 5a to facilitate comparison with the **g**-axis orientations of <sup>3</sup>P. The L half of the dimer is the upper bacteriochlorophyll in this depiction. The direction of the axis associated with the largest **g**-value remains virtually independent of temperature. SOC centered on the L-side ring I acetyl has been invoked to explain a similar rotation of the **g**-axes in P<sup>+</sup>.<sup>44</sup> This result suggests that SOC on the acetyl oxygen atom may be quite significant in determining rotation of the **g**-tensor in <sup>3</sup>P as a function of temperature.

The excellent agreement of calculated line shapes from both the RPM and YRM with the experimental data suggests that triplet yield anisotropy is by far the most likely source of the orientation-dependent intensity observed in the high-field <sup>3</sup>P EPR spectrum. However, there are other potential sources for this variation that will now briefly be considered. One possibility is photoselection, wherein excitation of the sample by polarized light produces an anisotropic distribution of triplet states relative to the optical transition dipole moment, which is fixed in the molecular frame.<sup>53</sup> Such effects are very unlikely in the present case, because it has been demonstrated that excitation at 532 nm is essentially isotropic because of the distribution of transition dipoles among the RC pigments at this wavelength.<sup>21</sup> A second possibility is alignment of the RCs in the PVA films resulting from the sample preparation procedure. However, examination of the dried PVA films under a polarizing microscope showed no evidence for alignment of the RCs, and the films comprising the sample were stacked randomly with respect to orientation.

A more significant possibility, given the relatively large integration period of 2  $\mu$ s (5  $\mu$ s at 30 K) used to collect the spectra, is anisotropic decay of the triplet signal. Anisotropic spin–lattice relaxation has been invoked to explain the unusual spin polarization pattern observed for <sup>3</sup>P in *R. viridis* RCs where the secondary quinone acceptor Q has been prereduced.<sup>54,55</sup> This anisotropic *T*<sub>1</sub> was attributed to interactions between <sup>3</sup>P and the Q<sup>•</sup>-Fe complex in these RCs. Such effects are not expected for the Q-removed RCs from *Rb. sphaeroides* used in the present study, because no anomalous spin polarization patterns have

been reported for <sup>3</sup>P this type of sample. Nevertheless, little is known about triplet *T*<sub>1</sub>'s at high field, and this remains a significant possibility.

To assess the effect of triplet decay anisotropy on the experimental line shape, decay times were determined from single-exponential fits to the raw time-domain data at the canonical orientations. A small anisotropy was indeed apparent from this analysis, with decay times ranging from 125  $\pm$  6  $\mu$ s near the high field Z feature to 70  $\pm$  5  $\mu$ s near the low field X feature at 30 K; and from 6  $\pm$  1 to 4  $\pm$  1  $\mu$ s near the same two positions respectively at 230 K. The maximum error in signal intensity due to this variation was estimated by comparing the integrals of single-exponential functions with the given minimum and maximum decay times from *t* = 0 to the specified integration period. The 5  $\mu$ s integration period leads to a difference of 1.6% in the integrated yield at 30 K, and the 2  $\mu$ s period leads to a difference of about 8.5% at 230 K. These errors are well within the experimental uncertainties reported for the yield ratios in Table 1 and cannot account for the large signal anisotropies observed. Thus, the major source of the experimental intensity variation must arise from yield anisotropy and not decay anisotropy.

The yield anisotropy parameters obtained from the least-squares analysis exhibit consistent, monotonic trends over the temperature range studied. Because *r*<sub>x</sub> < *r*<sub>y</sub> < 1 in all cases, the relative triplet yield is lowest when *X*||**B**<sub>0</sub> and highest when *Z*||**B**<sub>0</sub>. The temperature dependence of the yield anisotropy most likely results from changes in the rates of electron back-transfer from the precursor radical pair with temperature, particularly that of the singlet-correlated radical pair state, which competes with radical pair intersystem crossing.

According to the magnetic axis convention described above, the X axis lies along the *Q*<sub>y</sub> (i.e., the 870 nm transition) optical transition dipole of the molecule.<sup>56</sup> Thus, our result that *r*<sub>x</sub> < *r*<sub>y</sub> < 1 is quite consistent with the results of Boxer and co-workers,<sup>20,21</sup> who found that the triplet yield measured at 870 nm was lowest when the observation light was polarized parallel to the applied magnetic field (i.e., *X*||**B**<sub>0</sub>). In principle, more structural detail may be available from the EPR spectrum of <sup>3</sup>P because the yield anisotropy may be determined relative to all three zero-field axes, whereas the linear dichroism measurements refer only to the magnetic field direction.

Although the YRM quite satisfactorily accounts for all the observed features of the spectra below 100 K, it fails to account for some features of the spectra at higher temperatures. In particular, the spectrum exhibits noticeable deviations from the predicted line shape above 100 K, as indicated by the arrows in Figure 3. Such features could arise from a resonance effect in the  $\Delta$ **g** anisotropy of the precursor radical ion pair that produces dips in the triplet yield at orientations where  $\Delta$ **g** is close to zero. The increased prominence of the dips at higher temperatures could then be attributable to faster recombination of singlet-correlated radical pairs (*k*<sub>s</sub>), which competes more effectively with intersystem crossing and therefore increases the orientation selectivity. An alternative possibility is that the peaks may reflect a second, thermally populated triplet state with different zero-field splittings and **g**-tensor.<sup>57</sup> Although the analysis of single spectra at low-temperature using the RPM does not permit a definitive determination of the radical pair **g**-tensors, future careful characterization of the additional structure observed at high temperature may provide enough additional information to resolve much of this ambiguity.

## Conclusion

Transient 240 GHz EPR spectra of the primary donor triplet state  $^3\text{P}$  in bacterial RCs have yielded new information about the  $\mathbf{g}$ -tensor of this state, which differs significantly from previous measurements at 130 GHz and lower frequencies. A significant temperature variation of the  $^3\text{P}$   $\mathbf{g}$ -tensor was observed, which was ascribed to rotation of the  $\mathbf{g}$  principal axes with temperature. The  $\mathbf{g}$ -tensor of the  $^3\text{P}$  state thus differs significantly from that of the cation radical state  $\text{P}^+$ , reflecting important differences in the spin-orbit coupling and electronic distribution between two electronic states of the same molecule. The intensity of the  $T_0$ -polarized high-field spectrum is also orientation-dependent, reflecting triplet yield anisotropy that arises from  $\mathbf{g}$ -tensor anisotropy of the precursor radicals. Analysis of the yield anisotropy of single spectra at temperatures below 100 K using a radical pair model did not allow definitive assignment of radical pair parameters. However, detailed analysis of the additional structure that appears in the high-frequency spectra at higher temperatures is expected to furnish new structural information about the precursor radical pair state. The results demonstrate the general utility of high-field EPR for investigating photoexcited triplet states of organic molecules.

**Acknowledgment.** This work was supported by NSF CAREER award MCB 9600940 (D.E.B.) and by the NSF grant CHE-9601731 (J.v.T.). The work in the laboratory of H.A.F. is supported by grants from the National Institutes of Health (GM-30353) and the National Science Foundation (MCB-9816759). We gratefully acknowledge many helpful interactions with Dr. Stephen V. Kolaczkowski and Dr. Louis-Claude Brunel.

## References and Notes

- Budil, D. E.; Earle, K. A.; Lynch, W. B.; Freed, J. H. Electron paramagnetic resonance at 1 millimeter wavelengths. In *Advanced EPR: Applications in biology and biochemistry*; Hoff, A. J., Ed.; Elsevier: Amsterdam, 1989; pp 307–340.
- Smith, G. M.; Riedi, P. C. *Electron Paramagn. Reson.* **2000**, *17*, 164–204.
- Möbius, K. *Chem. Soc. Rev.* **2000**, *29*, 129–139.
- Bratt, P. J.; Rorher, M.; Krzystek, J.; Evans, M. C. W.; Brunel, L. C.; Angerhofer, A. *J. Phys. Chem. B* **1997**, *101*, 9686–9689.
- Bratt, P. J.; Ringo, E.; Hassan, A.; Van Tol, H.; Maniero, A.-L.; Brunel, L.-C.; Rohrer, M.; Bubenzer-Hange, C.; Scheer, H.; Angerhofer, A. *J. Phys. Chem. B* **1999**, *103*, 10973–10977.
- Bratt, P. J.; Poluektov, O. G.; Thurnauer, M. C.; Krzystek, J.; Brunel, L.-C.; Schrier, J.; Hsiao, Y.-W.; Zemer, M.; Angerhofer, A. *J. Phys. Chem. B* **2000**, *104*, 6973–6977.
- Prisner, T. F.; McDermott, A. E.; Un, S.; Norris, J. R.; Thurnauer, M. C.; Griffin, R. G. *Proc. Natl. Acad. Sci. U.S.A.* **1993**, *90*, 9485–8.
- MacMillan, F.; Hanley, J.; van der Weerd, L.; Kneupling, M.; Un, S.; Rutherford, A. W. *Biochemistry* **1997**, *36*, 9297–9303.
- Dorlet, P.; Rutherford, A. W.; Un, S. *Biochemistry* **2000**, *39*, 7826–7834.
- Calvo, R.; Isaacson, R. A.; Paddock, M. L.; Abresch, E. C.; Okamura, M. Y.; Maniero, A.-L.; Brunel, L.-C.; Feher, G. *J. Phys. Chem. B* **2001**, *105*, 4053–4057.
- Weber, S. *Electron Paramagn. Reson.* **2000**, *17*, 43–77.
- Hoff, A. J. Triplets: phosphorescence and magnetic resonance. *Light Emission in Plants and Bacteria*; Academic Press: New York, 1986.
- Angerhofer, A. In *Chlorophylls*; Scheer, H., Ed.; CRC Press: Boca Raton, FL, 1991; pp 945–991.
- Budil, D. E.; Thurnauer, M. C. *Biochim. Biophys. Acta* **1991**, *1057*, 1–41.
- Huber, M.; Doubinskii, A. A.; Kay, C. W. M.; Moebius, K. *Appl. Magn. Reson.* **1997**, *13*, 473–485.
- Lendzian, F.; Bittl, R.; Lubitz, W. *Photosynth. Res.* **1998**, *55*, 189–197.
- Zeng, R.; van Tol, J.; Deal, A.; Frank, H. A.; Budil, D. E. Spin-Orbit Coupling in the Primary Donor Triplet State in Photosynthetic Systems: Implications For High-Field EPR; 24th International EPR Symposium at the 43rd Rocky Mountain Conference on Analytical Chemistry, 2001; Denver, CO.
- Labahn, A.; Huber, M. *Appl. Magn. Reson.* **2001**, *21*, 381–387.
- Paschenko, S. V.; Gast, P.; Hoff, A. J. *Appl. Magn. Reson.* **2001**, *21*, 325–334.
- Boxer, S. G.; Chidsey, C. E. D.; Roelofs, M. G. *J. Am. Chem. Soc.* **1982**, *104*, 2674–5.
- Boxer, S. G.; Chidsey, C. E. D.; Roelofs, M. G. *Proc. Natl. Acad. Sci. U.S.A.* **1982**, *79*, 4632–6.
- Boxer, S. G.; Chidsey, C. E. D.; Roelofs, M. G. *Annu. Rev. Phys. Chem.* **1983**, *34*, 389–417.
- Wraight, C. A. *Biochim. Biophys. Acta* **1979**, *548*, 309–27.
- Okamura, M. Y.; Steiner, L. A.; Feher, G. *Biochemistry* **1974**, *13*, 1394–403.
- van Tol, J.; Brunel, L. C.; Angerhofer, A. *Appl. Magn. Reson.* **2001**, *21*, 335–340.
- Poole, C. P. *Electron spin resonance: a comprehensive treatise on experimental techniques*, 2nd ed.; Wiley: New York, 1983.
- Lesurf, J. C. G. *Millimetre-wave Optics, Devices, and Systems*; Adam Hilger: Bristol, PA, 1990.
- Goldsmith, P. F. *Quasioptical Systems*; IEEE Press/Chapman & Hall Publishers: Piscataway, NJ, 1998.
- The Math Works, I. *MATLAB*, 5.3.1 ed.; The Math Works, Inc.: Natick, MA, 1998.
- Zare, R. N. *Angular Momentum: Understanding Spatial Aspects in Chemistry and Physics*; John Wiley and Sons: New York, 1988.
- Hoff, A. J.; Proskuryakov, I. I. *Chem. Phys. Lett.* **1985**, *115*, 303–10.
- Aust, V.; Angerhofer, A.; Parot, P. H.; Violette, C. A.; Frank, H. A. *Chem. Phys. Lett.* **1990**, *173*, 439–42.
- Till, U.; Hore, P. J. *Mol. Phys.* **1997**, *90*, 289–296.
- Press, W. H.; Teukolsky, S. A.; Vetterling, W. T.; Flannery, B. P. *Numerical Recipes in C: The Art of Scientific Computing*, 2nd ed.; Cambridge University Press: New York, 1992.
- Seber, G. A. F.; Wild, C. J. *Nonlinear Regression*; Wiley-Interscience: New York, 1989.
- Thurnauer, M. C.; Katz, J. J.; Norris, J. R. *Proc. Natl. Acad. Sci. U.S.A.* **1975**, *72*, 3270–4.
- Norris, J. R.; Budil, D. E.; Gast, P.; Chang, C. H.; El-Kabbani, O.; Schiffer, M. *Proc. Natl. Acad. Sci. U.S.A.* **1989**, *86*, 4335–9.
- Prisner, T. F.; van der Est, A.; Bittl, R.; Lubitz, W.; Stehlik, D.; Moebius, K. *Chem. Phys.* **1995**, *194*, 361–70.
- Stowell, M. H.; McPhillips, T. M.; Rees, D. C.; Soltis, S. M.; Abresch, E.; Feher, G. *Science* **1997**, *276*, 812.
- Norris, J. R.; Bowman, M. K.; Budil, D. E.; Tang, J.; Wraight, C. A.; Closs, G. L. *Proc. Natl. Acad. Sci. U.S.A.* **1982**, *79*, 5532–6.
- Moehl, K. W.; Lous, E. J.; Hoff, A. J. *Chem. Phys. Lett.* **1985**, *121*, 22–7.
- McElroy, J. D.; Feher, G.; Mauzerall, D. C. *Biochim. Biophys. Acta* **1972**, *267*, 363–374.
- Tiede, D. M.; Prince, R. C.; Reed, G. H.; Dutton, P. L. *FEBS Lett.* **1976**, *65*, 301–4.
- Plato, M.; Moebius, K. *Chem. Phys.* **1995**, *197*, 289–95.
- Klette, R.; Toerring, J. T.; Plato, M.; Moebius, K.; Boenigk, B.; Lubitz, W. *J. Phys. Chem.* **1993**, *97*, 2015–20.
- Fajer, J.; Fujita, I.; Forman, A.; Hanson, L. K.; Craig, G. W.; Goff, D. A.; Kehres, L. A.; Smith, K. M. *J. Am. Chem. Soc.* **1983**, *105*, 3837–43.
- Plato, M.; Moebius, K.; Michel-Beyerle, M. E.; Bixon, M.; Jortner, J. *J. Am. Chem. Soc.* **1988**, *110*, 7279–85.
- Plato, M.; Lendzian, F.; Lubitz, W.; Moebius, K. Molecular Orbital Study of Electronic Asymmetry in Primary Donors of Bacterial Reaction Centers. In *The Photosynthetic Bacterial Reaction Center II. Structure, Spectroscopy, and Dynamics*; Breton, J., Vermeglio, A., Eds.; Plenum Press: New York, 1992; pp 109–118.
- Borovykh, I. V.; Proskuryakov, I. I.; Klenina, I. B.; Gast, P.; Hoff, A. J. *J. Phys. Chem. B* **2000**, *104*, 4222–4228.
- Scherer, P. O. J.; Fischer, S. F.; Hoerber, J. K. H.; Michel-Beyerle, M. E.; Michel, H. *Springer Ser. Chem. Phys.* **1985**, *42*, 131–7.
- Raja, N.; Reddy, S.; Kolaczkowski, S. V.; Small, G. J. *Science* **1993**, *260*, 68–71.
- Angerhofer, A.; Bornhauser, F.; Aust, V.; Hartwich, G.; Scheer, H. *Biochim. Biophys. Acta* **1998**, *1365*, 404–420.
- McGlynn, S. P.; Azumi, T.; Kinoshita, M. *Molecular spectroscopy of the triplet state*; Prentice Hall: Eaglewood Cliffs, NJ, 1969; Chapter 5.
- van den Brink, J. S.; Manikowski, H.; Gast, P.; Hoff, A. J. *Biochim. Biophys. Acta* **1994**, *1185*, 177–87.
- van den Brink, J. S.; Gast, P.; Hoff, A. J.; Manikowski, H. *Appl. Magn. Reson.* **1994**, *6*, 67–81.
- Zinth, W.; Knapp, E. W.; Fischer, S. F.; Kaiser, W.; Deisenhofer, J.; Michel, H. *Chem. Phys. Lett.* **1985**, *119*, 1–4.
- Pachtchenko, S. V. Primary electron donor triplet states in photosynthetic reaction centers as studied by high-field EPR. Ph.D., University of Leiden, 2002.